Energy Advances

ROYAL SOCIETY OF CHEMISTRY

PAPER

View Article Online
View Journal

Cite this: DOI: 10.1039/d6ya00064a

Valorisation of wastewater sludge into activated carbon *via* H_3PO_4 activation for supercapacitor applications

Mojeed O. Bello, *[a] Ntuthuko W. Hlongwa, [a] Abolanle S. Adekunle[b] and Moshawe J. Madito *[a]

Received 4th March 2026,
Accepted 8th June 2026

DOI: 10.1039/d6ya00064a

rsc.li/energy-advances

The valorisation of wastewater sludge (WWS) into high-value functional materials offers a sustainable route to address waste management and energy storage challenges. In this work, WWS was converted into activated carbon (WSAC-H) *via* a single-step carbonisation process using 30% H_3PO_4 as the activating agent at 600 °C for 4 h. Structural and surface analyses revealed a rough, functionalised morphology and well-developed porosity. Electrochemical evaluation in a three-electrode system showed that 1 M H_2SO_4 yielded the highest specific capacitance (114.96 F g^{-1} at 0.5 A g^{-1}), outperforming 1 M Na_2SO_4 (41.40 F g^{-1}) and 1 M KOH (18.04 F g^{-1}) at the same current density. A symmetric device in 1 M H_2SO_4 delivered an energy density of 5.89 Wh kg^{-1} and a power density of 1000 W kg^{-1} at 0.5 A g^{-1}, retaining 84% of its capacitance after 20 000 charge–discharge cycles at 3.0 A g^{-1}. The performance is attributed to the synergistic effects of acid activation, intrinsic elemental composition, and high electrolyte conductivity. These findings demonstrate the potential of WWS-derived activated carbon as a cost-effective, high-performance supercapacitor electrode material, advancing both environmental remediation and sustainable energy storage.

Introduction

The generation of wastewater sludge (WWS) has increased substantially in recent years due to urbanisation, industrial activity, and the growing demand for potable water. Although global statistics are incomplete, it is estimated that approximately 53 million tonnes of dried sludge are produced annually, based on reported data from individual countries.[1] In South Africa, the expansion of urban water cycles to meet drinking water needs has significantly increased sludge production from wastewater treatment plants (WWTPs). Managing this large and complex waste stream is challenging due to its heterogeneous composition, potential for environmental contamination, and the limited capacity of conventional disposal routes such as landfilling or agricultural application.[2–4] Addressing this issue requires environmentally sustainable, cost-effective strategies that not only reduce sludge volumes but also recover value from the waste. One promising approach is to convert WWS into carbon-based materials for use in energy storage devices. Such valorisation addresses two pressing concerns: waste management and the global shift towards cleaner, renewable energy technologies.

The intermittent nature of renewable energy sources such as solar, wind, and tidal power necessitates efficient and reliable energy storage solutions. Among available technologies, supercapacitors (electrochemical capacitors) have attracted considerable attention for their combination of high power density, rapid charge–discharge performance, cycle life, and operational safety.[5,6] Their ability to deliver high power density and long cycle life (up to millions of cycles) makes them particularly suited for applications ranging from portable electronics to grid stabilisation.

The energy storage mechanism of supercapacitors is governed by either electric double-layer capacitance (EDLC), arising from electrostatic charge accumulation at the electrode/electrolyte interface, or pseudocapacitance, involving fast, reversible redox reactions on the electrode surface.[7–9] EDLCs typically employ carbon-based electrodes, such as activated carbon or graphene, whereas pseudocapacitors utilise transition-metal oxides or conducting polymers.[10,11] While supercapacitors excel in power delivery and cycling stability, they often exhibit lower energy density than batteries and face challenges such as self-discharge and higher material costs.[12–16] These limitations can be mitigated by optimising both electrode materials and electrolyte composition.

[a] Institute for Nanotechnology and Water Sustainability (iNanoWS), College of Science, Engineering and Technology (CSET), University of South Africa, Johannesburg, 1710, South Africa. E-mail: bellomo@unisa.ac.za, maditmj@unisa.ac.za

[b] Institute for Catalysis and Energy Solutions (ICES), College of Science, Engineering and Technology (CSET), University of South Africa, Johannesburg, 1710, South Africa

Aqueous electrolytes are widely used for their high ionic conductivity and low cost. They can be classified as acidic (*e.g.*, H_2SO_4), alkaline (*e.g.*, KOH, NaOH), or neutral (*e.g.*, Na_2SO_4, KCl).[17,18] Acidic electrolytes, such as H_2SO_4, provide high conductivity and small ionic size, enhancing capacitance, though with a limited voltage window (~1.2 V) and corrosiveness.[19,20] Alkaline electrolytes can offer a wider potential range and good conductivity, but are strongly influenced by cation size and electrode-surface interactions.[21] Neutral electrolytes are safer and allow for broader voltage ranges, but generally exhibit lower conductivity.[18,22] Organic and ionic-liquid electrolytes extend the voltage window further, thereby increasing energy density, but are less conductive and more costly.[23]

In recent years, sewage sludge has been investigated as a low-cost precursor for activated carbon electrodes in supercapacitors. Such sludge-derived carbons can exhibit high specific surface areas, hierarchical porosity, and favourable conductivity, particularly when processed *via* pyrolysis, chemical activation, or heteroatom doping. Studies have reported competitive electrochemical performance for these materials,[24,25] yet opportunities for optimisation remain. In particular, the role of activation conditions, especially acid activation in a single-step carbonisation, and the effect of different aqueous electrolytes on capacitive behaviour have not been fully explored.

In this study, we synthesise activated carbon from wastewater sludge using 30% orthophosphoric acid (H_3PO_4) in a single-step carbonisation at 600 °C. We systematically investigate its physicochemical characteristics (surface area, morphology, elemental composition, functional groups) and electrochemical performance in acidic (H_2SO_4), alkaline (KOH), and neutral (Na_2SO_4) aqueous electrolytes. Performance is assessed in both three-electrode and symmetric two-electrode configurations, with emphasis on cycling stability and charge-storage mechanisms. By correlating electrolyte properties with capacitance, energy/power density, and stability, this work aims to advance the sustainable use of WWS-derived carbons in high-performance supercapacitor applications.

Results and discussion

Physicochemical properties

The XRD patterns of WWS and WSAC-H, along with reference patterns from the Inorganic Crystal Structure Database (ICSD): card no. 31170 (hexagonal carbon; space group: *P*63*mc*), 8096 (monoclinic SiP_2O_7; space group: *P*121/*n*1), 34889 (tetragonal SiO_2; space group: P43212), and 18164 (tetragonal $CaCO_3$; space group: $R\bar{3}c$) for peak indexing and phase identification is presented in Fig. 1a. The colour coding of each indexed phase histogram corresponds to the colour of the labelled diffraction planes for that phase. The XRD pattern of raw WWS is dominated by crystalline calcite ($CaCO_3$, main peaks at 2θ = 29.3° and 31.0°) and quartz (SiO_2, main peak at 2θ = 26.3°). Minor peaks may correspond to hematite (Fe_2O_3) and/or magnetite (Fe_3O_4), anhydrite ($CaSO_4$), and lime (CaO), which likely originate from ferric salts and lime used during wastewater treatment. In contrast, the XRD pattern of WSAC-H is characterised by prominent diffraction peaks at 2θ = 20.3°, 22.9°, 23.8°, 26.4°, 27.5°, 30.4°, 33.1°, 37.3°, 38.0°, and 42.8°, associated with SiP_2O_7, as well as peaks at 25.8° and 28.9° corresponding to SiO_2. A broad hump near 26° 2θ, typically indicative of amorphous carbon, is obscured by overlapping crystalline peaks. The presence of SiP_2O_7 confirms that the silica in WWS reacted with phosphoric acid during activation, producing chemically

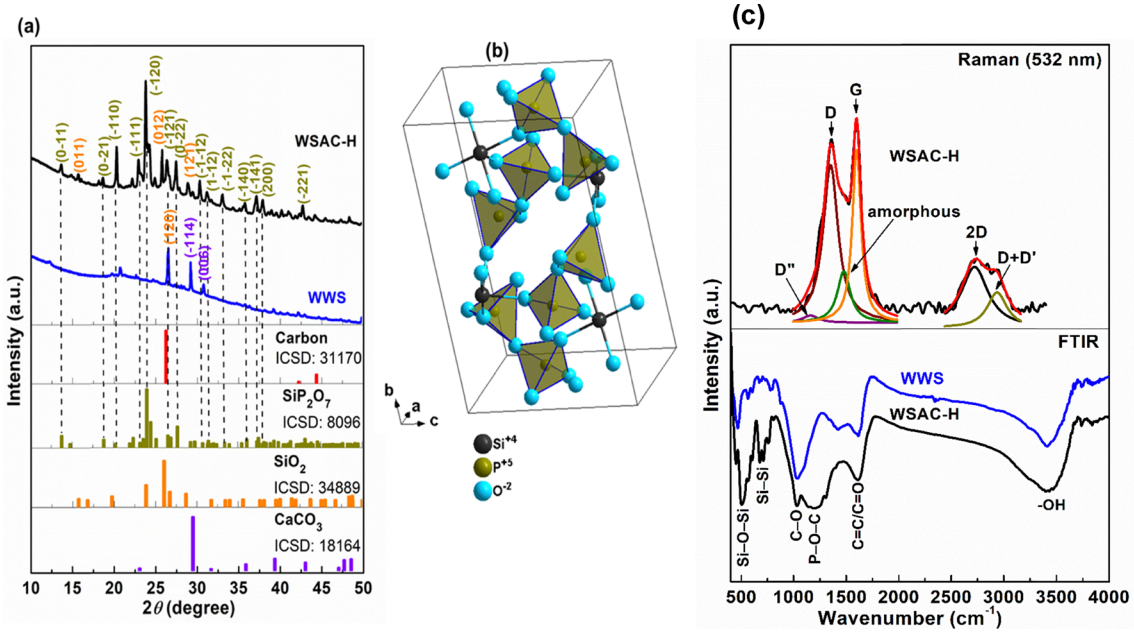

Fig. 1 (a) XRD patterns of WWS and WSAC-H with reference patterns from ICSD (b) crystalline SiP_2O_7 unit cell obtained using ICSD card no. 8096 and Diamond software version 5.1.0 (c) FTIR spectrum of WWS and WSAC-H together with the Raman spectrum of WSAC-H.

stable crystalline silicophosphates. Structurally (Fig. 1(b)), crystalline SiP_2O_7 consists of Si atoms bonded to six O atoms to form SiO_6 octahedra, each sharing corners with six PO_4 tetrahedra. The Si–O bond distances range from 0.173 to 0.177 nm. Phosphorus atoms are bonded to four O atoms to form PO_4 tetrahedra, each sharing corners with three SiO_6 octahedra and one PO_4 tetrahedron. The P–O bond distances range from 0.150 to 0.159 nm. The strong Si–P–O covalent bonds contribute to the high chemical stability of the SiP_2O_7 framework, thereby enhancing structural integrity, preserving the porous carbon architecture during long-term cycling, and improving surface wettability, facilitating electrolyte penetration and ion transport into the carbon pores.

The surface functionalities of the WWS and WSAC-H were examined using FTIR spectroscopy (Fig. 1c). Both materials display a broad –OH stretching band at 3413 cm^{-1}, attributed to hydroxyl groups from phenols, alcohols, or adsorbed water molecules.[26,27] The absorption band near 1615 cm^{-1} corresponds to aromatic C=C stretching within sp^2-hybridised graphitic structures, indicating the presence of condensed aromatic domains and may overlap with conjugated C=O groups. The band observed around 1037 cm^{-1} is attributed to C–O stretching vibrations of oxygen-containing functional groups, such as alcohols, phenols, ethers, and ester moieties on the activated carbon surface.[28] Activation with H_3PO_4 induced notable structural changes, including the appearance of a band around 1190 cm^{-1}, assigned to P–O–C linkages (P=O in phosphate esters, P=OOH bonds, and P–O–P vibrations), confirming the incorporation of phosphorus into the activated carbon framework.[29] Additional bands at $\sim$510 and $\sim$710 cm^{-1} are attributed to Si–O–Si and Si–Si vibrations, respectively, representing residual inorganic constituents from the raw wastewater sludge.

Raman spectroscopy further elucidates the structural characteristics of WSAC-H (Fig. 1c). The spectrum shows prominent D (1356 cm^{-1}) and G (1603 cm^{-1}) bands, along with a broad band near 2900 cm^{-1} (*i.e.*, 2D at $\sim$2700 cm^{-1} and D + D′ at $\sim$2950 cm^{-1}), providing insight into the defect density, graphitic ordering, and degree of amorphisation. In addition to the characteristic D and G bands, a broad Raman feature at $\sim$1500 cm^{-1} is often attributed to amorphous carbon.[30] The G band arises from in-plane optical phonons (in-plane C–C bond stretching) with E_{2g} symmetry at the Γ point.[31] In contrast, the D band (and D″ band at $\sim$1150 cm^{-1}) is defect-activated, appearing only when disorder disrupts translational symmetry. The 2D band's shape and intensity are sensitive to stacking order and the number of carbon layers, serving as key indicators of graphitisation and interlayer coupling.[31] The measured I(D)/I(G) intensity ratio of 0.90 and I(2D)/I(G) ratio of $\sim$0.35 indicate a predominantly disordered carbon structure containing embedded graphitic sp^2 domains. The in-plane crystallite size (L_a) was estimated to be $\sim$5.5 nm using the Tuinstra-Koenig relation.[31] An I(D)/I(G) ratio close to unity, combined with a weak and broad 2D band (I(2D)/I(G) $\approx$ 0.35), is characteristic of carbon materials with low graphitisation, confirming that WSAC-H exhibits a low degree of graphitic ordering.

The surface morphological properties and the elemental compositions of the WWS and the obtained WSAC-H are shown in Fig. 2a and b. The surface morphology of WWS (Fig. 2a insert) consists of a network of coarsely aggregated irregular particles that are highly diverse. These irregularly shaped particles agglomerate into larger secondary particles, resulting in a rugged, cauliflower-like texture with numerous voids and crevices. In comparison, the image of WSAC-H (Fig. 2b insert) also shows heterogeneous, irregular particles, including both smaller crystalline particles and surface agglomerates. This observation may result from the activation and carbonisation processes. The result is similar to the SEM image of raw and activated carbon of municipal sewage sludge reported by Almahbashi *et al.* and Mezhevova *et al.*[32,33]

Regarding elemental composition, energy-dispersive X-ray spectroscopy reveals that both the raw sludge and the activated carbon contain carbon, oxygen, calcium, silicon, and aluminium (Fig. 2a and b). The sludge has a low initial carbon content, which results in low carbon content in the activated carbon. The amount of carbon in activated carbon depends on the quantity present in its precursor.[32] This amount decreases due to burning off during the carbonisation process. Thus, the carbon content in WSAC-H is less than in WWS. Additionally, burning off results in the loss of some elements (Ca, Mg, and Fe) initially present in WWS. The presence of phosphorus in the elemental composition of the activated carbon (WSAC-H) reflects the influence of the orthophosphoric acid (H_3PO_4) used as the activating agent.

The microstructural features of the samples were examined using TEM and SAED, as presented in Fig. 2c and d. WWS (Fig. 2c) exhibits thin, rippled, and partially stacked nanosheets with discernible lattice fringes, indicating a relatively ordered layered structure. In contrast, WSAC-H (Fig. 2d) reveals a more fragmented, loosely packed nanosheet network composed of smaller, irregular flakes, reflecting a higher degree of structural disorder and mesoporous properties. The observation is consistent with the Raman analysis results for the WSAC-H.

The SAED patterns further confirm the observations from TEM images. The raw sludge, WWS (Fig. 2c insert), exhibits sharp, well-defined diffraction spots arranged in concentric rings, characteristic of polycrystalline ordering within the nanosheets. This is likely due to the presence of several metals in the sludge, as indicated by the EDX results. Conversely, WSAC-H (Fig. 2d insert) shows broad, diffuse halo rings with no distinct spots, indicating an amorphous or poorly crystalline framework. The transition from ordered to disordered structure in WASC-H may be attributed to the H_3PO_4 activation and carbonisation processes, which can disrupt long-range order. Such structural differences are expected to influence the electrochemical behaviour of the materials, particularly with respect to ion transport and charge-storage efficiency.[34]

The N_2 adsorption–desorption isotherms and the corresponding BJH pore volume curve for WSAC-H are shown in Fig. 2e. The isotherms display a characteristic Type IV shape with an H3 hysteresis loop in the relative pressure range of 0.45 to 1.0, which is representative of mesoporous materials

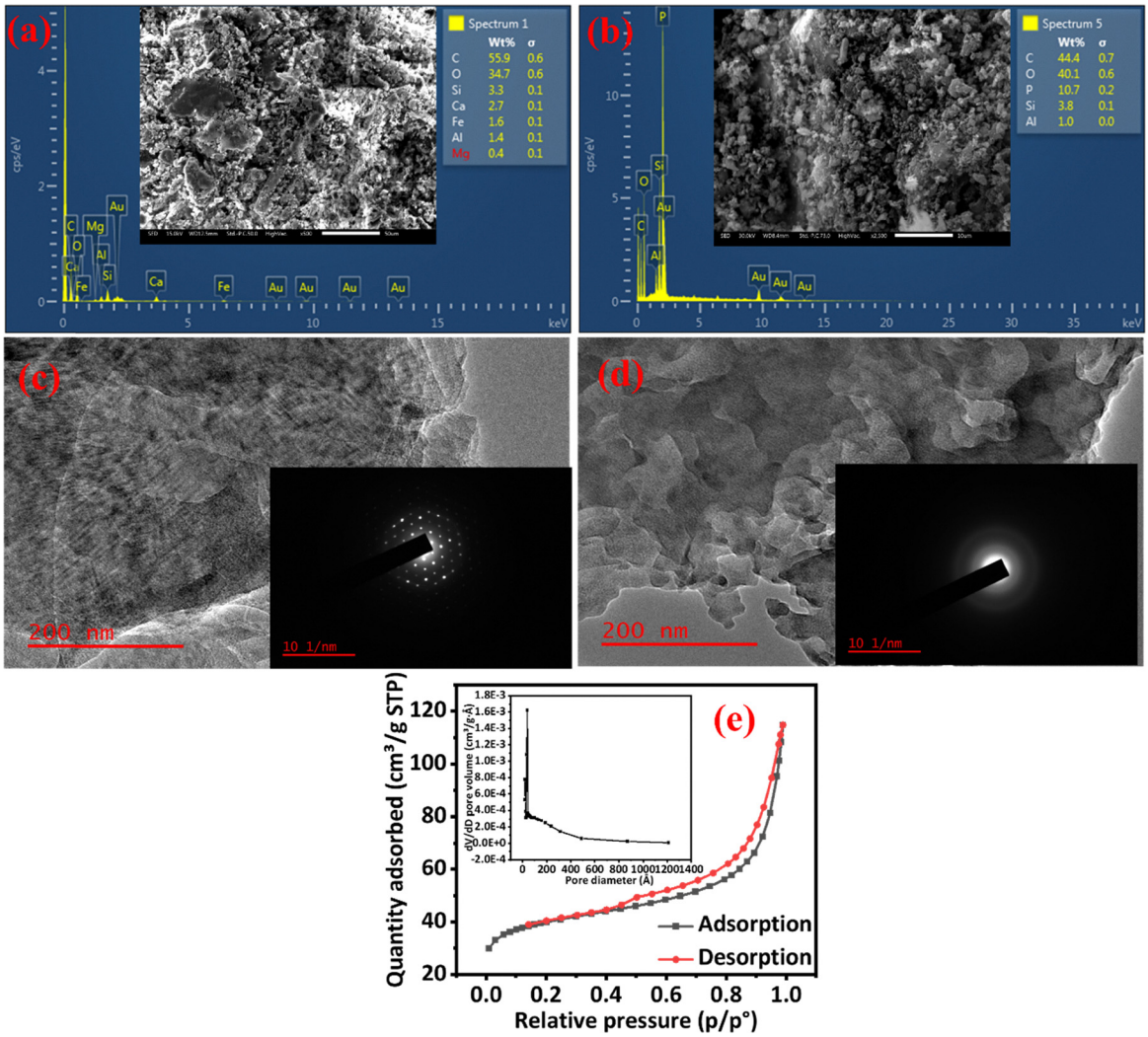

Fig. 2 SEM image and EDX spectrum of (a) WWS and (b) WSAC-H; TEM image and SEAD of (c) WWS and (d) WSAC-H, and (e) BET analysis of WSAC-H.

containing slit-like pores. The calculated BET surface area and total pore volume were approximately 134.23 $m^2\ g^{-1}$ and 0.128 $cm^3\ g^{-1}$, respectively. Furthermore, the BJH pore-size distribution (Fig. 2e insert) exhibits a narrow peak at 35.7 Å (3.57 nm), confirming the presence of a well-defined mesoporous framework. These textural characteristics, particularly the surface area and accessible mesopores, are expected to facilitate electrochemical performances.[35]

Electrochemical properties

Three-electrode system

The cyclic voltammetry (CV) of the WSAC-H in three different electrolytes, 1 M H_2SO_4, 1 M KOH, and 1 M Na_2SO_4 in a three-electrode system, is presented in this section. For optimisation, the CV was conducted over a range of scan rates from 2 to 100 mV s^{-1}, as depicted in Fig. 3a–c. The CV in 1 M H_2SO_4 and 1 M Na_2SO_4 within a potential window of 0.9 V shows a quasi-rectangular shape, indicating electric double-layer capacitance (EDLC) behaviour, a common observation in materials such as activated carbon.[36] At a relatively high scan rate (100 mV s^{-1}), the material retains its electrochemical properties, suggesting rapid charge transport and strong ionic/electronic conductivity.[37] A quasi-rectangular shape of the EDLC was observed at a low scan rate of 2 mV s^{-1} in 1 M KOH, but its EDLC nature was distorted as the scan rate was increased from 5 to 100 mV s^{-1} within a potential window of 0.4 V. The deviation from the ideal shape may be due to an increase in charge-transfer resistance as the scan rate increases.[38,39] The distortion can also result from the neutralisation of K^+ and OH^- by residual acid activator as the scan rate increases, thereby limiting ion diffusion within the porous carbon structure and restricting electrolyte ion accessibility, compared with H_2SO_4 and Na_2SO_4 of the same concentration.

The specific capacitance (C_{sp}) (F g^{-1}) from the CV curves for the WSAC-H electrode in the three (3) electrolytes is presented in Fig. 3d. It is observed that the capacitance decreases with an increase in the scan rate for the three electrolytes. The highest capacitance of 100.8 F g^{-1} was observed in 1 M H_2SO_4, followed by 1 M Na_2SO_4 (46 F g^{-1}) and 1 M KOH (27 F g^{-1}) at 2 mV s^{-1}. At

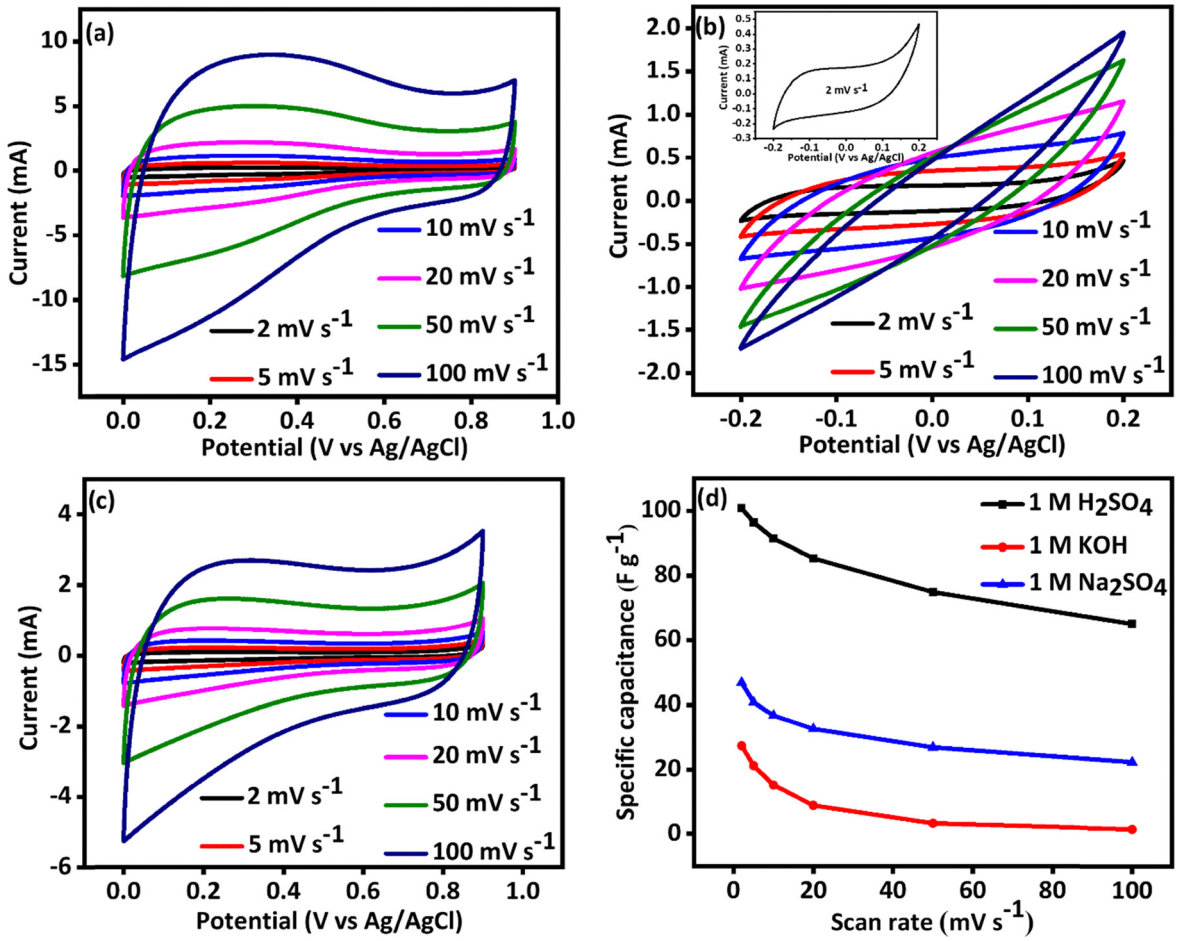

Fig. 3 CV plots of WSAC-H in (a) 1 M H_2SO_4 (b) 1 M KOH (c) 1 M Na_2SO_4, and (d) specific capacitance (F g^{-1}) at different scan rates.

higher scan rates, charge–discharge occurred too quickly for complete ion diffusion. Therefore, less of the electrode surface was utilised, resulting in a lower specific capacitance.[40] Whereas, lower scan rates allow ions to reach the most inaccessible sites of the electrode, resulting in higher specific capacitance[41,42]

The galvanostatic charge–discharge (GCD) analyses of WASC-H in the three electrolytes at various current densities are shown in Fig. 4a–c. GCD analysis is an important electrochemical technique for evaluating the electrochemical performance of supercapacitor materials, based on charge/discharge time and electrical conductivity.[40,43] Generally, the specific capacitance decreases with increasing current density, as depicted in Fig. 4d. WSAC-H exhibited the longest discharge time and the highest specific capacitance at lower current densities. This is due to the greater time available for electrolyte ions to move through the electrode material. Consequently, complete and efficient charge storage results in higher capacitance in the process.[44] It is believed that the active electrode material (WSAC-H) exhibited different behaviours across the three electrolytes, resulting in differences in specific capacitance. At 0.5 A g^{-1} current density, the obtained specific capacity is in the order of 1 M KOH (18.04 F g^{-1}) < 1 M Na_2SO_4 (41.40 F g^{-1}) < 1 M H_2SO_4 (114.96 F g^{-1}). According to the theory, the order of conductivity is 1 M Na_2SO_4 < 1 M KOH < 1 M H_2SO_4, which is expected to have a great impact on capacitance. Energy is stored in supercapacitors through the electrostatic adsorption of ions at the interface between the electrode and electrolyte (electric double layer).[45] Higher ionic conductivity allows ions to move faster and more freely through the electrolyte to the electrode surface. Similarly, mobility, conductivity, and performance are influenced by the size of the cation in the electrolyte. The cationic sizes are in the order of H^+ (0.115 Å) < Na^+ (0.90 Å) < K^+ (1.33 Å).[46,47] Therefore, the performance of WSAC-H in 1 M H_2SO_4 is better than in 1 M KOH and Na_2SO_4 due to its high conductivity and small, fast-moving H^+ ions. The presence of residual acid (H_3PO_4) used during wastewater sludge activation before carbonisation, which is also present in the pores of the activated carbon, might enhance conductivity in 1 M H_2SO_4 but neutralise the strength of 1 M KOH. The consequence of the neutralisation of the 1 M KOH, together with the size of K^+, is likely the narrow potential window observed. Higher capacitance, along with a higher potential window, is required for supercapacitors.[48] The ionic equations and the observed conductivities of the three electrolytes are given in eqn (1)–(3).

$$H_2SO_4 \rightleftharpoons 2H^+ + SO_4^{2-} = 426.80 \text{ mS cm}^{-1} \quad (1)$$

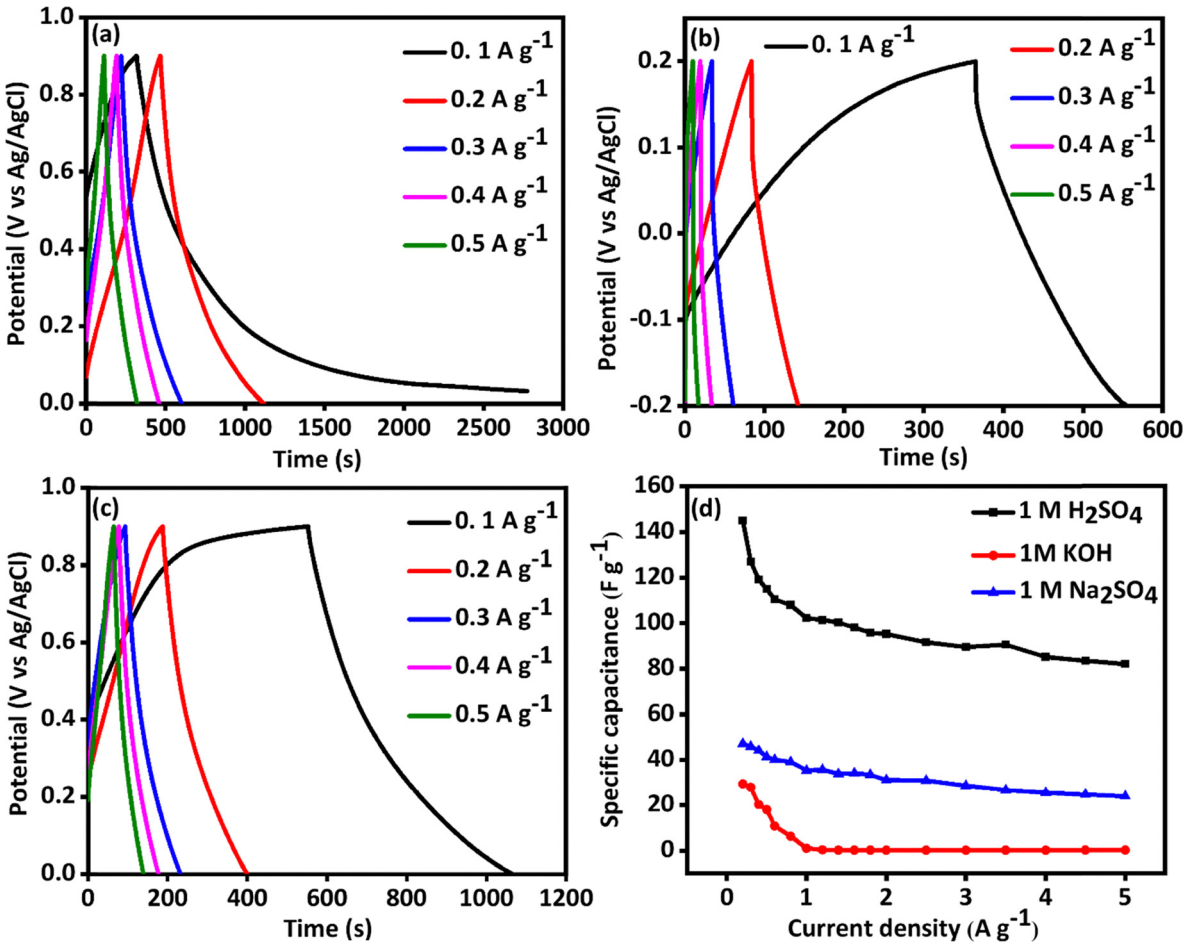

Fig. 4 GCD plots of WSAC-H in (a) 1 M H_2SO_4 (b) 1 M KOH (c) 1 M Na_2SO_4 and (d) Specific capacitance (F g^{-1}) at different current densities.

$$KOH \rightleftharpoons K^+ + OH^- = 174.95 \text{ mS cm}^{-1} \quad (2)$$

$$Na_2SO_4 \rightleftharpoons 2Na^+ + SO_4^{2-} = 88.18 \text{ mS cm}^{-1} \quad (3)$$

The Nyquist plots of electrochemical impedance spectroscopy (EIS) for the three systems, namely WSAC-H in 1 M H_2SO_4, 1 M KOH, and 1 M Na_2SO_4, measured between 0.1 and 100 mHz, are depicted in Fig. 5a–c. The plots show the physical components, including solution resistance (R_s), charge-transfer resistance (R_{ct}), and double-layer capacitance (C_{dl}).[24,49] Using *Z* fit function on BioLogic software (EC-Lab V11.50) to fit the experimental data, the equivalent circuit revealed other components such as a Warburg element (*W*) and a constant phase element (CPE). From the equivalent circuit fitting, low R_s and R_{ct} were observed for WSAC-H in 1 M H_2SO_4 and 1 M Na_2SO_4, compared with those in 1 M KOH (Table 1). This indicates efficient charge transfer at the electrode/electrolyte interface and fast charge transfer kinetics,[50–52] especially in 1 M H_2SO_4. Similarly, the presence of the Warburg element indicates ion diffusion limitation within the electrode pores, implying that the system deviates from ideal capacitive behaviour.[53] The Warburg coefficient follows the trend 1 M H_2SO_4 < 1 M Na_2SO_4 < 1 M KOH, indicating that a smaller cation size leads to faster ion transport at the electrode/electrolyte interface. Warburg coefficient is inversely proportional to the square root of the diffusion coefficient. The presence of CPE captures the surface heterogeneity, electrode roughness, overlap between double-layer charging and possible pseudocapacitive contributions, which cannot be distinctly resolved within the investigated frequency range.[54,55]

The charge storage behaviour of WSAC-H in each of the three electrolytes (1 M H_2SO_4, 1 M KOH, and 1 M Na_2SO_4) is further investigated using the obtained cyclic voltammetry data at different scan rates (2 to 100 mV s^{-1}). A plot of a power law describes the total storage mechanism as a combination of capacitive and diffusion-controlled processes.[56] Reports have pointed out that b = 0.5 indicates a diffusion-controlled process, whereas b = 1.0 indicates a surface-controlled process.[24,56] It is observed that the storage process is characterised by both surface and diffusive control in 1 M H_2SO_4 and 1 M Na_2SO_4, as indicated by the b values from the plot of log (i) *vs.* log (v) (Fig. 6a), which fall between 0.5 and 1.0. Consequently, it was highly imperative to investigate the contribution of each mechanism. It is noteworthy that the electrochemical data for WSAC-H in 1 KOH didn't fit the power-law equation because the system became unstable as the scan rate increased.

The percentage contribution of each storage mechanism for WSAC-H in 1 M H_2SO_4 and 1 M Na_2SO_4 is shown in Fig. 6b and c, respectively. The surface-controlled mechanism increases, and the diffusion-controlled mechanism decreases as the scan rate

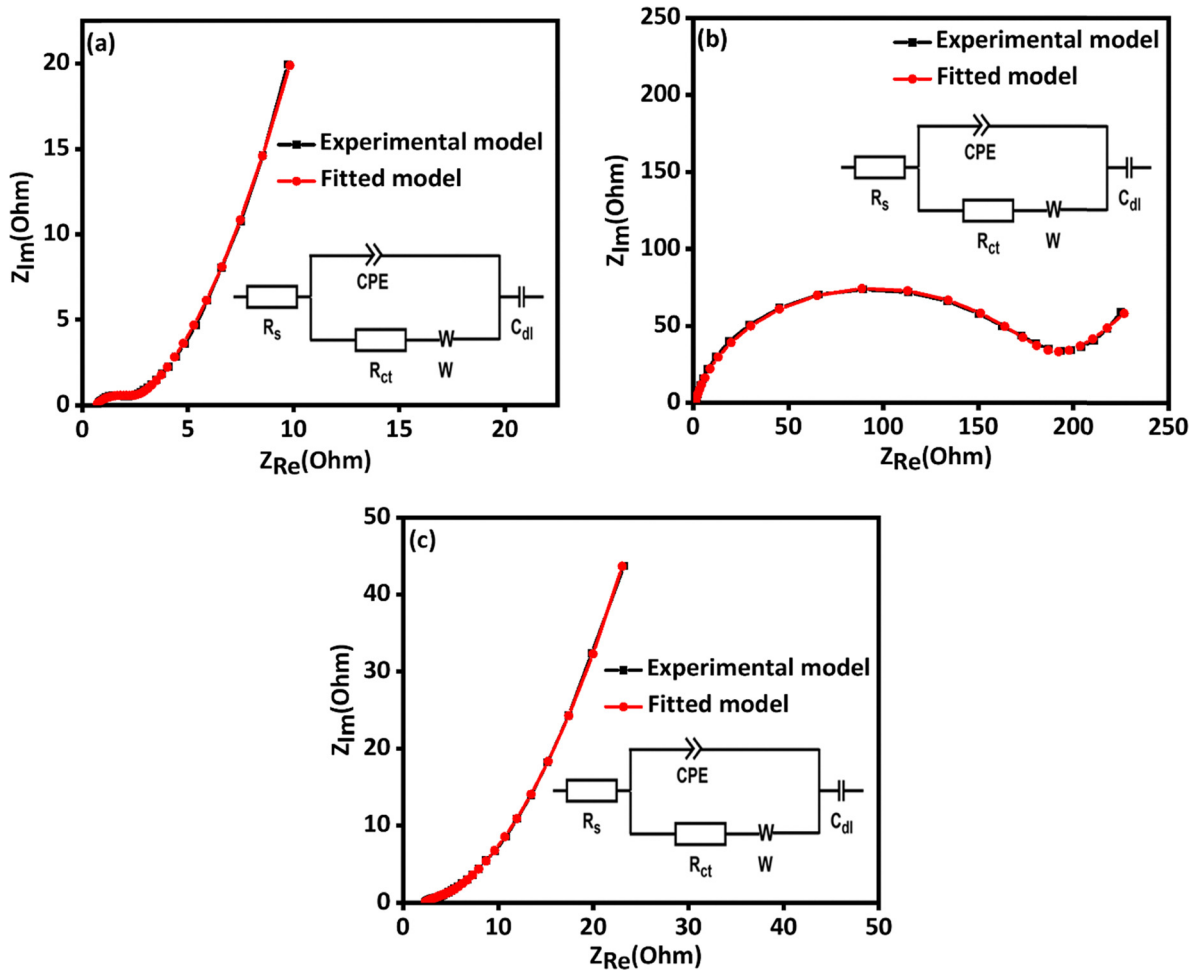

Fig. 5 Nyquist plots of WSAC-H in (a) 1 M H_2SO_4 (b) 1 M KOH, and (c) 1 M Na_2SO_4.

Table 1 EIS parameters of WSAC-H in different electrolytes for the three-electrode system

	Parameter				
System	R_s (Ω)	R_{ct} (Ω)	C_{dl} (F)	CPE (F $s^{(n-1)}$)	W (Ω $s^{-1/2}$)
1 M H_2SO_4	0.63	2.01	0.13	3.3×10^{-3}	5.96
1 M KOH	0.99	179.7	0.24	1.1×10^{-4}	38.32
1 M Na_2SO_4	2.15	5.69	0.05	0.02	26.30

increases. It has been established that electrolyte ions carrying charges do not have enough time to travel into the inner parts of the electrode at higher scan rates, but are retained at the surface, thereby favouring a surface-controlled mechanism.[57,58] This percentage contribution ratio at 10 mV s^{-1} is shown in Fig. 6d and e, imaging in the cyclic voltammogram.

Symmetrical device fabrication

The true performance of an electrode material is revealed through the electrochemical properties measured during device fabrication, that is, in a two-electrode system. Herein, a symmetrical device was assembled and tested to determine electrochemical properties using cyclic voltammetry, galvanostatic charge–discharge, and electrochemical impedance spectroscopy. The best-performing electrolyte in the three-electrode system, that is, 1 M H_2SO_4, was investigated here. Fig. 7(a) shows the CV results of the fabricated WSAC-H device in 1 M H_2SO_4 at various scan rates (2–100 mV s^{-1}) within a slightly wider potential window (1 V) than in three-electrode mode (0.9 V). The CV curve for the devices is more rectangular than that for the three-electrode system. This suggests a largely surface-controlled (capacitive) charge mechanism. The CV demonstrates an increasing enclosed area while retaining its shape and stability within the potential window as the scan rate increases. The observation demonstrated a real EDLC behaviour of a carbon-based electrode.

The GCD plot of the WSAC-H device in 1 M H_2SO_4 at some current densities, within a range of 0.1 and 5.0 A g^{-1}, is represented in Fig. 7b. The triangular shape obtained, as depicted, indicates ideal capacitive behaviour. It signifies that the device stores charges through electrostatic accumulation at the electrode/electrolyte interface.[59,60] This is greatly influenced by the nature of the electrode material, such as activated carbon, which tends to demonstrate more EDLC behaviour and charge-transport properties of the electrolyte.[61,62] The specific

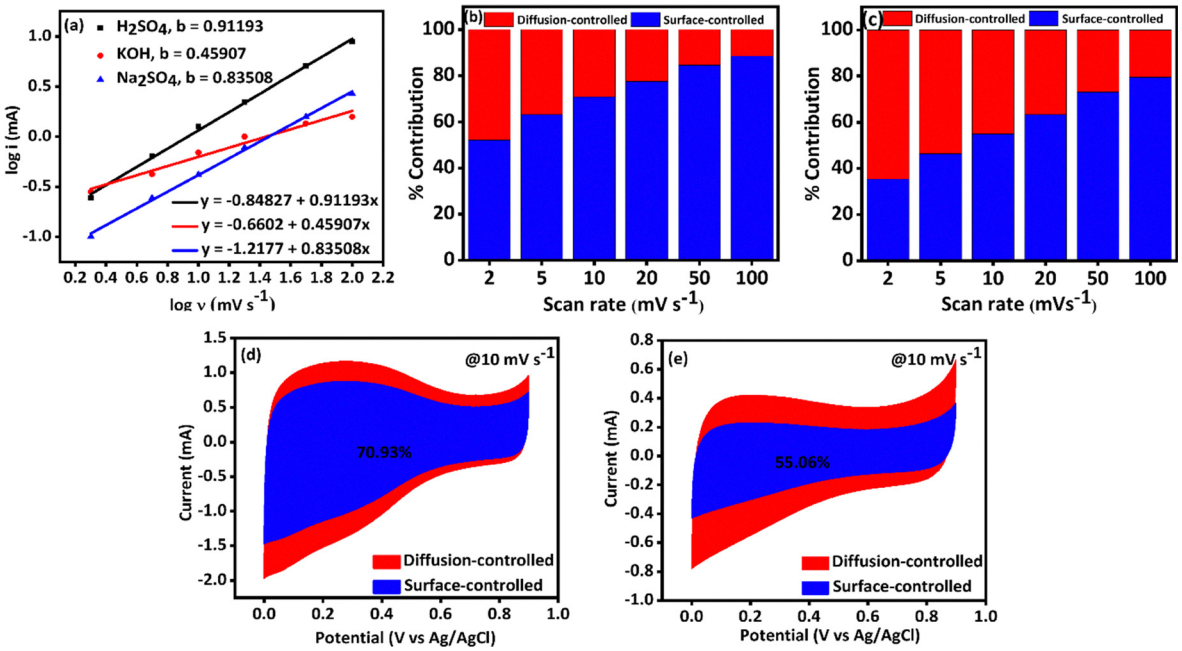

Fig. 6 (a) Plot of log current *vs.* log scan rate, (b) and (c) are percentage contributions of storage mechanism in 1 M H_2SO_4 and 1 M Na_2SO_4, respectively, (d) and (e) are percentage contributions at 10 mV s^{-1} in the voltammogram for 1 M H_2SO_4 and 1 M Na_2SO_4, respectively.

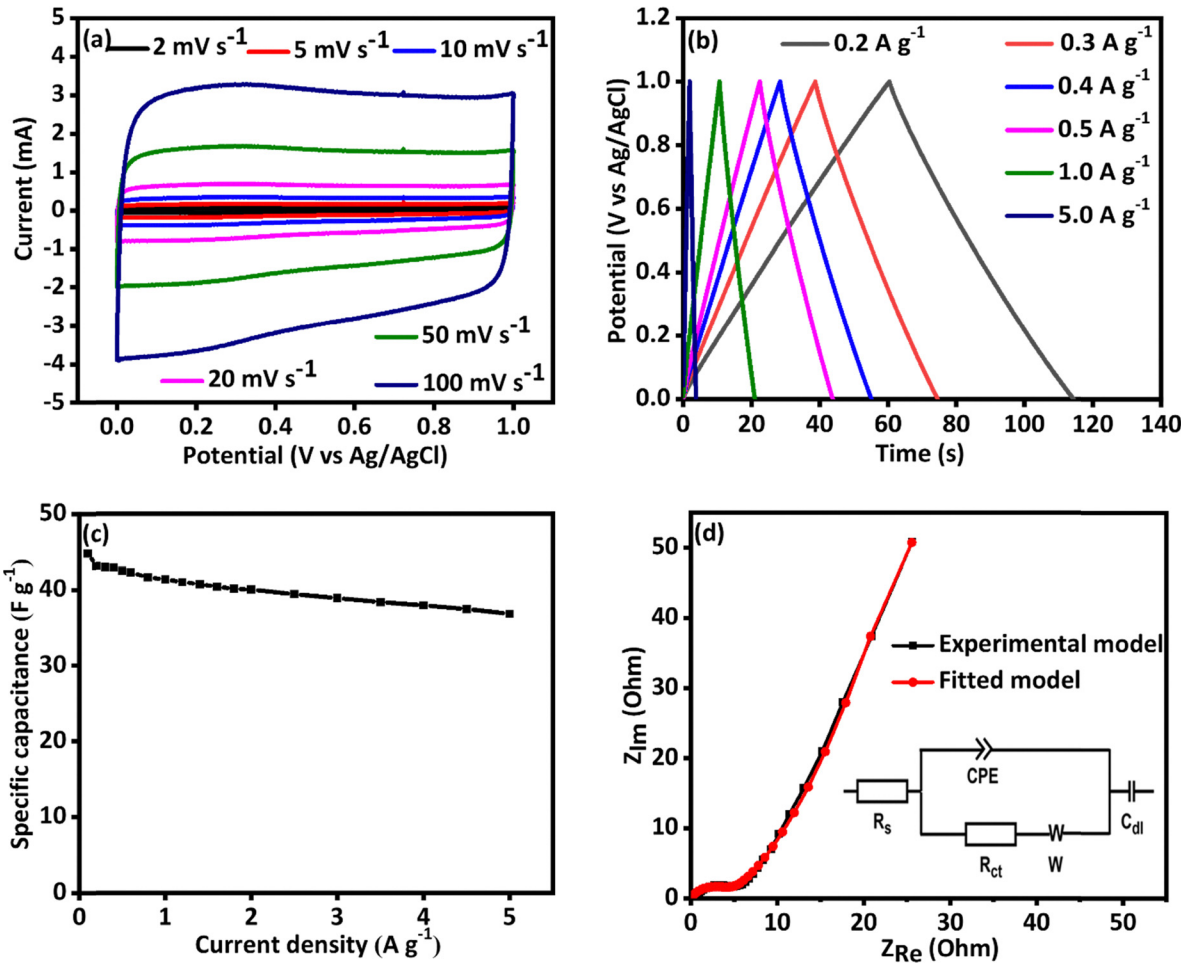

Fig. 7 (a) CV (b) GCD (c) specific capacitance and (d) Nyquist plot of the device WSAC-H in 1 M H_2SO_4.

Table 2 EIS parameters of the symmetrical WSAC-H in a 1 M H_2SO_4 device

Model	Parameters				
	R_s (Ω)	R_{ct} (Ω)	C_{dl} (F)	CPE (F $s^{(n-1)}$)	W (Ω $s^{-1/2}$)
Experimental model	0.352	5.56	—	—	—
Fitted model	0.43	4.02	0.05	2.90×10^{-4}	15.84

capacitance (C_{sp}) in the device was estimated using eqn 5b. Similarly to the three-electrode system, the specific capacitance (C_{sp}) decreases with increasing current density (Fig. 7c). The values of C_{sp} at 0.2, 0.5, 1.0, and 5.0 A g^{-1} are 43.12, 42.46, 41.60, and 36.80 F g^{-1}, respectively. These values demonstrate a significant specific capacitance at higher current densities. A summary of the electrochemical performance at 0.5 A g^{-1}, compared with relevant reports, is presented in Table 3.

To determine the kinetics of charge transfer and characterise the electrochemical reaction process, electrochemical impedance spectroscopy (EIS) is another crucial technique. Fig. 7d shows the Nyquist plot obtained from the EIS analysis of the fabricated devices. The plot shows a small solution resistance (R_s), a charge-transfer resistance (R_{ct}), a constant-phase element, and a Warburg diffusion element (W). Low R_s and R_{ct} values of 0.352 Ω and 5.56 Ω, respectively, were measured experimentally, suggesting that the system exhibits excellent electrode/electrolyte interactions and favourable charge-transport properties.[63] The experimental data were fitted to an appropriate circuit using Z fit in BioLogic EC software. As shown in Table 2, the R_s and R_{ct} values from the fit closely match the experimental values, indicating a good Z fit. The fitted model also revealed that C_{dl}, CPE and Warburg coefficient were 0.05 F, 2.90×10^{-4} F $s^{(n-1)}$ and 15.84 Ω $s^{-1/2}$, respectively. CPE is an imperfect capacitive phenomenon (deviation from ideal behaviour) as a result of a heterogeneous energy level or a rough surface of the electrode material.[54,64] The nature of the wastewater sludge (WWS) precursor and the elemental composition of the resulting activated carbon, as revealed by the physicochemical characterisation, may have contributed to this occurrence.

Another important property of a supercapacitor device is its cycling stability. Here, the cycling stability of WSAC-H in 1 M H_2SO_4 was tested over 20 000 cycles at a current density of 3.0 A g^{-1}, with EIS measurements taken every 5000 cycles. Fig. 8a shows the capacitance retention (%) and coulombic efficiency (%) against cycle count, along with the corresponding charge–discharge process (inserts). Over 20 000 cycles, the device retained 83.43% of its specific capacitance and maintained 100% coulombic efficiency. It demonstrates a stable charge–discharge process over time.[65] This significant stability and percentage capacitance retention are attributed to the synergistic action of the H_3PO_4-activated carbon, as well as to the elemental composition, such as Al, Si, and Fe, present in its precursor and the acidic electrolyte. The 16.57% decrease in specific capacitance retention between the first and 20 000th cycle was monitored with EIS measurements at every 5000th cycle (Fig. 8b). It is physically evident that the R_{ct}, the diameter of the semi-circle, increases, suggesting the difficulty the charges encounter when transferring across the electrolyte/electrode interface as the number of stability cycles increases. The fitted value of the experimental Nyquist plot indicated R_{ct} values of 1.00 Ω, 1.46 Ω, 2.05 Ω, and 3.65 Ω for the 1st, 2nd, 3rd, and 4th 5000 cycles, respectively. This observation is a likely consequence of electrolyte degradation or a change in electrode morphology.[66]

To further assess the efficiency of the symmetrical WSAC-H device in 1 M H_2SO_4, a Ragone curve is plotted (Fig. 8c), showing the relationship between specific energy and power at various current densities. The device achieves an energy density of 5.89 Wh kg^{-1} and a power density of 1000 W kg^{-1} at 0.5 A g^{-1}. These values remain 5.11 Wh kg^{-1} and 10 000 W kg^{-1} for energy density and power density, respectively, at 5.0 A g^{-1}. The result further demonstrates the superior stability of WSAC-H produced from wastewater sludge as a supercapacitor electrode material at relatively high current densities.

Experimental

Materials

Wastewater sludge (WWS) was collected from two municipal wastewater treatment facilities in South Africa: Northern Works Wastewater Treatment Works (Johannesburg) and Daspoort Wastewater Treatment Works (Pretoria). The sludge, a

Table 3 Electrochemical performance of WSAC-H compared with previously reported values for similar materials

S/N	Source	Activating agent/method	Electrolyte	Specific capacitance	Energy density (Wh kg^{-1})	Power density (W kg^{-1})	Ref.
1	Water filter	KOH	1 H_2SO_4	122.8@1 A g^{-1}	15.4	936.6	67
			1 Na_2SO_4	81.2@1 A g^{-1}	32.9	1767	25
2.	Wastewater treatment plant	KOH/Hydrothermal	6 M KOH	76.72@0.25 A g^{-1}	6.14	64	25
3	Paper mill	KOH/Hydrothermal	3 M KOH 1 M Na_2SO_4	125@0.5 A g^{-1}	17.4	200	24
				152@0.5 A g^{-1}	21.1	200	
4.	Petrochemical industry	$ZnCl_2$/One-step carbonisation	6 M KOH	281.7	—	—	68
5.	Textile	H_3PO_4/Hydrothermal	2 M KOH	83.2@1 A g^{-1}	—	—	69
7	Wastewater treatment plant	H_3PO_4/One-step carbonisation	1 M H_2SO4	114.96@0.5 A g^{-1}			This work
			1 M KOH	18.04@0.5 A g^{-1}			
			1 M Na_2SO_4	41.40@0.5 A g^{-1}			
			1 M H_2SO_4 (Device)	42.46@0.5 A g^{-1}	5.89	1000	

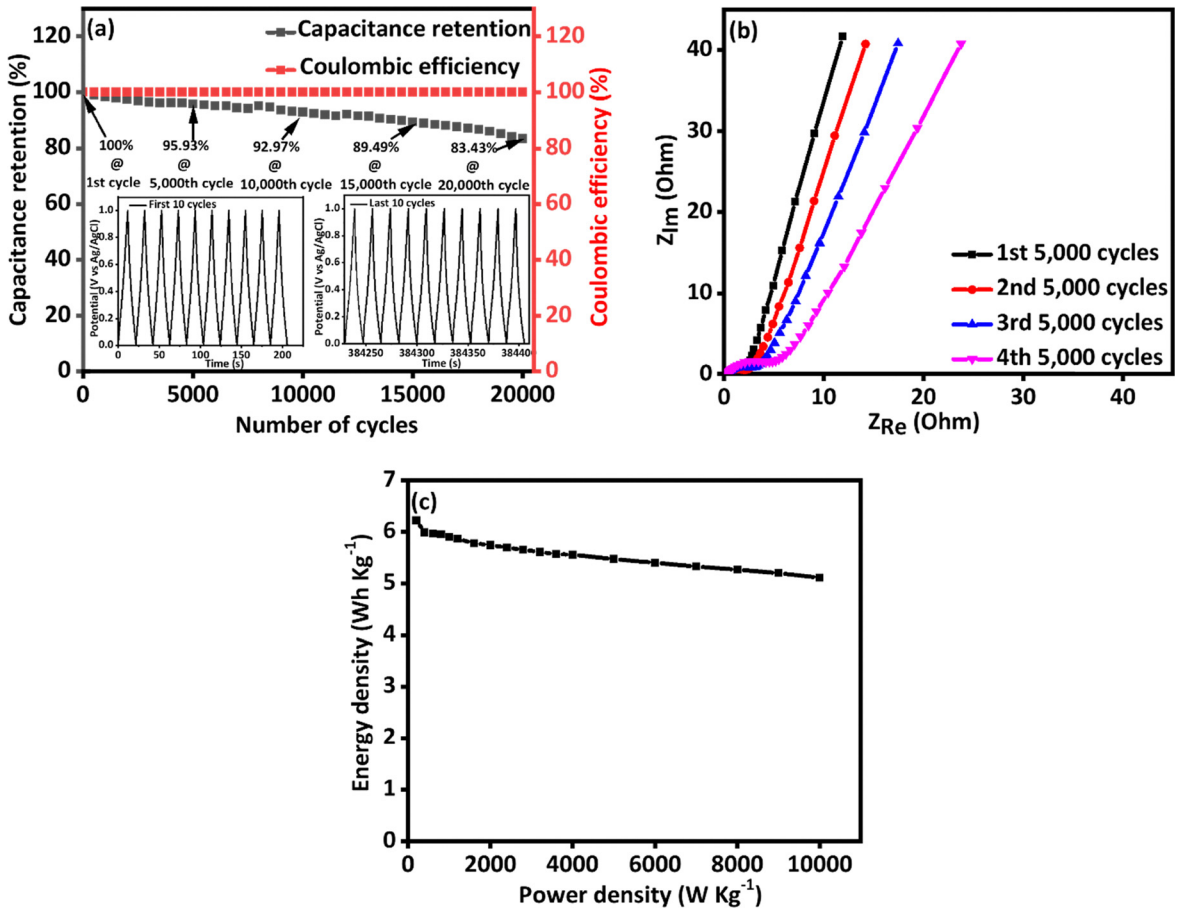

Fig. 8 (a) % Capacitance retention in 20 000 cycles (b) Nyquist plots after every 5000 cycles, and (c) Ragone plot of the device.

waste by-product, was transferred into polyethylene bags using a shovel and stored at ambient temperature before use.

All chemicals used were of analytical grade and procured from a reputable commercial supplier. Orthophosphoric acid (H_3PO_4, 30% v/v) served as the activating agent. Additional chemicals included polyvinylidene fluoride (PVDF), N-methyl-2-pyrrolidone (NMP), carbon black, hydrochloric acid (HCl), acetone, and ethanol. Deionised (DI) water was used for all washing and cleaning steps.

Methods

Initial characterisation of sludge

Before activation, the as-collected WWS was air-dried and analysed to determine its initial chemical composition. The single-step carbonisation method reported by Bello *et al.*[70] was adopted with slight modifications. Briefly, dried WWS was impregnated with 30% H_3PO_4 at a sludge-to-acid ratio of 1 : 10 (w/v) and soaked for 18 h to allow for thorough chemical penetration. The material was subsequently washed, dried, and carbonised in a Lenton muffle furnace at 600 °C for 4 h under an inert atmosphere. The resulting product, tagged wastewater sludge-activated carbon (WSAC-H), was repeatedly washed with DI water to remove residual acid and soluble impurities, oven-dried at 105 °C, pulverised, and sieved to a uniform particle size. The powdered material was stored in airtight containers for further analysis and electrode fabrication.

Physicochemical characterisation

The morphological, structural, and spectroscopic properties of WWS and WSAC-H were characterised using multiple techniques. Raman spectroscopy with a WiTec confocal Raman microscope was employed to assess crystallinity. Fourier-transform infrared spectroscopy (FTIR, PerkinElmer Spotlight 400) was used to characterise surface functional groups. X-ray diffraction (XRD, Rigaku diffractometer) with Cu Kα radiation (λ = 0.154 nm) and a 2θ range of 5–80° was used for phase identification. Scanning electron microscopy coupled with energy-dispersive X-ray spectroscopy (SEM-EDX, JSM IT-300) was employed to characterise surface morphology and elemental composition. Transmission electron microscopy and selected area electron diffraction were performed using a TEM JEOL JEM-2100F operating at 200kV. The specific surface area and pore properties were determined using the Brunauer–Emmett–Teller (BET) method and analysed with Micromeritics ASAP 2460 version 4.00.

Electrode fabrication and electrochemical measurements

Stainless steel (SS, Grade 304, 0.1 mm thick) sheets were used as current collectors. Before electrode coating, the SS substrates

were sequentially ultrasonically cleaned for 30 min in 3 M HCl, acetone, and ethanol, then rinsed with DI water and dried under ambient conditions. The electrode slurry was prepared by mixing WSAC-H, carbon black, and polyvinylidene fluoride (PVDF) in an 8 : 1 : 1 mass ratio, using N-methyl-2-pyrrolidone (NMP) as the dispersing solvent. The homogeneous slurry was uniformly coated onto a 1 cm × 1 cm SS substrate and oven-dried at 80 °C for 8 h to ensure binder adhesion and complete solvent removal.

Electrochemical characterisation was conducted on an electrochemical workstation (BioLogic SP-300) in both three-electrode and symmetric two-electrode configurations. In the three-electrode configuration, the WSAC-H-coated stainless steel substrate served as the working electrode, a platinum plate as the counter electrode, and an Ag/AgCl electrode as the reference. The electrolyte was either 1 M H_2SO_4, 1 M KOH, or 1 M Na_2SO_4. Cyclic voltammetry (CV), galvanostatic charge–discharge (GCD), and electrochemical impedance spectroscopy (EIS) were performed for each electrolyte. For the symmetric two-electrode configuration, both electrodes were identical WSAC-H-coated SS substrates, assembled with a porous separator, and tested in the best-performing electrolyte (1 M H_2SO_4) identified in the three-electrode studies.

All electrochemical parameters were calculated from CV, GCD, and EIS measurements using the following equations.[40,71]

Specific capacitance, $C_{sp'}$ (F g^{-1}) from CV

$$C_{sp} = \frac{A}{2 \times k \times m \times V} \quad (4)$$

and from GCD:

$$C_{sp,(3\ electrodes)} = \frac{I \times \Delta t}{m \times \Delta V} \quad (5a)$$

$$C_{sp,(2\ electrodes)} = 4\frac{I \times \Delta t}{m \times \Delta V} \quad (5b)$$

where A is the integrated area under the CV curve (A V), k is the scan rate (V s^{-1}), m is the active mass of electrode material (g), I is the current (A), ΔV is the potential window (V), and Δt is the discharge time (s).

Energy density, E_d, (Wh kg^{-1}) and power density, P_d, (W kg^{-1}) are given by

$$E_d = \frac{C_{sp,(2\ electrode)} \times V^2}{2 \times 3.6}, \quad (6)$$

$$P_d = \frac{3600 \times E_d}{\Delta t}. \quad (7)$$

Moreover, the contributions from capacitive and diffusion-controlled processes were evaluated using the power-law relationship of Dunn's method:

$$i = av^b \quad (8a)$$

$$\log i = \log a + b \log v \quad (8b)$$

where i is the current (A) at a given potential, ν is the scan rate (mV s^{-1}), a is an adjustable constant, and b is an exponent indicating the dominant mechanism. A value of $b = 0.5$ corresponds to diffusion control, $b = 1$ indicates surface capacitive dominance, and intermediate values suggest a mixed mechanism.

The capacitive and diffusion contributions were further calculated and separated using:

$$i(V) = k_1\nu + k_2\nu^{0.5} \quad (9a)$$

$$\frac{i_{(V)}}{\nu^{0.5}} = k_1\nu^{0.5} + k_2 \quad (9b)$$

where k_1 and k_2 represent constants associated with capacitive and diffusion-controlled charge storage, respectively.

Capacitance retention, C_R (%) and coulombic efficiency, η (%) as a function of cycle number were calculated using eqn (10) and (11), respectively.

$$C_R = \frac{C_n}{C_i} \times 100 \quad (10)$$

$$\eta = \frac{t_d}{t_c} \times 100 \quad (11)$$

where C_i, C_n, t_c and t_d are the initial capacitance, the capacitance at n cycles, the charging time, and the discharging time, respectively.

Conclusions

In conclusion, activated carbon was successfully prepared from wastewater treatment sludge using H_3PO_4 as an activating agent *via* a single-step carbonisation process. Physicochemical characterisation by BET analysis confirmed a good specific surface area and well-developed microporosity, while SEM and FTIR revealed a rough surface with functional groups that facilitate ion adsorption. Electrochemical tests in a three-electrode setup investigating the effect of electrolytes on the performance of WSAC-H as supercapacitor materials revealed that it performed exceptionally well in 1 M H_2SO_4, with a specific capacitance of 114.96 F g^{-1} at 0.5 A g^{-1}, compared to 1 M KOH and 1 M Na_2SO_4. The assembled symmetric device in 1 M H_2SO_4 demonstrated an energy density of 5.89 Wh kg^{-1} and a power density of 1000 W kg^{-1} at 0.5 A g^{-1}. The device also showed impressive cycling stability at 3.0 A g^{-1}, maintaining 84.34% of its initial capacitance after 20 000 cycles. These impressive properties are attributed to the synergistic effects of acid (H_3PO_4) activated carbon, the initial elemental composition of the wastewater sludge precursor, and the compatibility and conductivity of the acidic electrolyte. These findings emphasise the potential of wastewater sludge to be converted into activated carbon through a single-step carbonisation process using H_3PO_4 as an activating agent, making it a high-performance electrode material for sustainable energy storage devices.

Author contributions

Moshawe J. Madito: conceptualisation, data curation, software, visualisation, validation, writing – review & editing, supervision. Adekunle S. Adekunle: writing – review & editing, validation. Ntuthuko W. Hlongwa: writing – review & editing, validation.

Mojeed O. Bello: investigation, methodology, writing – original draft, formal analysis,data curation, visualisation.

Conflicts of interest

There are no conflicts to declare.

Data availability

Data are available from the authors upon request.

Acknowledgements

The authors acknowledge the University of South Africa for the postdoctoral fellowship awarded to Dr Mojeed O. Bello. They also thank the Institute for Nanotechnology and Water Sustainability (iNanoWS) for providing the necessary research facilities.

References

1 J. Feng, I. T. Burke, X. Chen and D. I. Stewart, *Rev. Environ. Sci. Biotechnol.*, 2023, **22**, 1037–1058.
2 A. Rorat, P. Courtois, F. Vandenbulcke and S. Lemiere, *Industrial and Municipal Sludge: Emerging Concerns and Scope for Resource Recovery*, 2019, pp. 155–180.
3 S. Shaddel, H. Bakhtiary-Davijany, C. Kabbe, F. Dadgar and S. W. Østerhus, *Sustainability*, 2019, 3435.
4 M. K. H. Winkler, C. Meunier, O. Henriet, J. Mahillon, M. E. Suárez-Ojeda, G. Del Moro, M. De Sanctis, C. Di Iaconi and D. G. Weissbrodt, *Chem. Eng. J.*, 2018, **336**, 489–502.
5 S. Moraveji, L. Fotouhi, S. Shahrokhian and M. Zirak, *Sci. Rep.*, 2025, **15**, 1–15.
6 C. V. V. Muralee Gopi, S. Alzahmi, V. Narayanaswamy, K. V. G. Raghavendra, B. Issa and I. M. Obaidat, *Mater. Horizons*, 2025, **12**, 4092–4132.
7 K. B. Ansari, R. Mashkoor, M. A. Naim, A. R. Shakeelur Raheman, M. Y. Ansari, P. Khan, R. Hasib and M. Shkir, *J. Energy Storage*, 2025, **112**, 115564.
8 M. Heydari Gharahcheshmeh and K. Chowdhury, *Energy Adv.*, 2024, **3**, 2668–2703.
9 A. Patel, S. K. Patel, R. S. Singh and R. P. Patel, *Discover Nano*, 2024, **19**, 188.
10 A. G. Olabi, Q. Abbas, M. A. Abdelkareem, A. H. Alami, M. Mirzaeian and E. T. Sayed, *Batteries*, 2023, DOI: 10.3390/batteries9010019.
11 A. Tundwal, H. Kumar, B. J. Binoj, R. Sharma, G. Kumar, R. Kumari, A. Dhayal, A. Yadav, D. Singh and P. Kumar, *RSC Adv.*, 2024, **14**, 9406–9439.
12 S. Karthikeyan, B. Narenthiran, A. Sivanantham, L. D. Bhatlu and T. Maridurai, *Mater. Today Proc.*, 2020, **46**, 3984–3988.
13 H. A. Khan, M. Tawalbeh, B. Aljawrneh, W. Abuwatfa, A. Al-Othman, H. Sadeghifar and A. G. Olabi, *Energy*, 2024, DOI: 10.1016/j.energy.2024.131043.
14 J. Libich, J. Máca, J. Vondrák, O. Čech and M. Sedlaříková, *J. Energy Storage*, 2018, **17**, 224–227.
15 Sonia, Reenu, A. Kumar L. Phor and S. Chahal, *J. Energy Storage*, 2024, DOI: 10.1016/j.est.2024.110698.
16 W. Shang, W. Yu, X. Xiao, Y. Ma, Y. He, Z. Zhao and P. Tan, *Adv. Powder Mater.*, 2023, DOI: 10.1016/j.apmate.2022.100075.
17 M. S. El Halimi, A. Zanelli, F. Soavi and T. Chafik, *World*, 2023, **4**, 431–449.
18 R. Ramachandran and F. Wang, *Supercapacitors - Theoretical and Practical Solutions*, 2018.
19 Q. Gao, L. Demarconnay, E. Raymundo-Piñero and F. Béguin, *Energy Environ. Sci.*, 2012, **5**, 9611–9617.
20 E. Taer, Agustino, Awitdrus, Apriwandi, A. Amri, R. Taslim and Zulkifli, *Curr. Top. Electrochem.*, 2021, **23**, 73–80.
21 A. Muzaffar, M. B. Ahamed and C. M. Hussain, *Smart Supercapacitors: Fundamentals, Structures, and Applications*, Elsevier, 2022, pp. 227–254.
22 R. Rohith, A. T. Prasannakumar, V. Manju, M. Thomas, R. R. Mohan and S. J. Varma, *Electrochim. Acta*, 2024, **503**, 144911.
23 H. V. T. Nguyen, A. Bin Faheem and K. K. Lee, *J. Power Sources*, 2025, **638**, 236455.
24 J. Abdulsalam, K. Otun, N. Gardee, B. Patel, T. Leswifi and M. K. Mathe, *ACS Omega*, 2023, **8**, 5285–5299.
25 O. S. Djandja, F. G. Kong, L. X. Yin, P. G. Duan, D. Xu and K. Kapusta, *Biomass Bioenergy*, 2022, **163**, 106526.
26 P. Wiercik, M. Kuśnierz, M. Kabsch-Korbutowicz, A. Plucińska and P. Chrobot, *Desalin. Water Treat.*, 2022, **273**, 114–125.
27 D. Shrestha, S. Maensiri, U. Wongpratat, S. W. Lee and A. R. Nyachhyon, *J. Environ. Chem. Eng.*, 2019, 103227.
28 N. Bouchelkia, K. Benazouz, A. Mameri, L. Belkhiri, N. Hamri, H. Belkacemi, A. Zoukel, A. Amrane, F. Aoulmi and L. Mouni, *Processes*, 2023, 2694.
29 A. Damayanti, R. Wulansarie, Z. A. S. Bahlawan, Suharta, M. Royana, M. W. N. M. Basuki, B. Nugroho and A. L. Andri, *ChemEngineering*, 2023, 75.
30 A. Sadezky, H. Muckenhuber, H. Grothe, R. Niessner and U. Pöschl, *Carbon*, 2005, **43**, 1731–1742.
31 A. C. Ferrari and D. M. Basko, *Nat. Nanotechnol.*, 2013, DOI: 10.1038/nnano.2013.46.
32 N. M. Y. Al-mahbashi, S. R. M. Kutty, A. H. Jagaba, A. Al-nini, A. T. Sholagberu, B. N. S. Aldhawi and U. Rathnayake, *Case Stud. Chem. Environ. Eng.*, 2023, 100437.
33 A. S. Mezhevova, Y. V. Berestneva and A. M. Pugacheva, *Ecol. Ind. Russ.*, 2021, 14–20.
34 T. Guo, P. Hu, L. Li, Z. Wang and L. Guo, *Chem*, 2023, DOI: 10.1016/j.chempr.2023.03.032.
35 Z.-Y. Bai, Z.-X. Wan-Me, P. Liu, F. Yang, L.-J. Sun, Y.-M. Jia and Y.-L. Xie, *J. Power Sources*, 2026, 238774, DOI: 10.1016/j.jpowsour.2025.238774.
36 C. H. Kwak, D. Kim and B. C. Bai, *Molecules*, 2022, 1454.
37 X. Zhang, L. Gao, R. Guo, M. Ma and T. Hu, *Appl. Surf. Sci.*, 2022, 151458.
38 N. Lima, A. C. Baptista, B. M. M. Faustino, S. Taborda, A. Marques and I. Ferreira, *Sci. Rep.*, 2020, 7703.
39 K. K. Yadav, R. Wadhwa, N. Khan and M. Jha, *Curr. Res. Green Sustainability Chem.*, 2021, 100075.
40 K. Gajewska, A. Moyseowicz, D. Minta and G. Gryglewicz, *J. Mater. Sci.*, 2023, **58**, 1721–1738.

41 Y. Luo, T. Yang, Z. Li, B. Xiao and M. Zhang, *Mater. Lett.*, 2016, **178**, 171–174.
42 B. Pattanayak, P. A. Le, D. Panda, F. M. Simanjuntak, K. H. Wei, T. Winie and T. Y. Tseng, *RSC Adv.*, 2022, 27082–27093.
43 H. D. Asfaw, A. Kucernak, E. S. Greenhalgh and M. S. P. Shaffer, *Compos. Sci. Technol.*, 2023, 110042.
44 S. Alkhalaf, C. K. Ranaweera, P. K. Kahol, K. Siam, H. Adhikari, S. R. Mishra, F. Perez, B. K. Gupta, K. Ramasamy and R. K. Gupta, *J. Alloys Compd.*, 2017, **692**, 59–66.
45 G. Z. Chen, *Int. Mater. Rev.*, 2017, DOI: 10.1080/09506608.2016.1240914.
46 R. Manikandan, C. J. Raj, M. Rajesh, B. C. Kim, J. Y. Sim and K. H. Yu, *ChemElectroChem*, 2018, **5**, 101–111.
47 A. Mendhe and H. S. Panda, *Discovery Mater.*, 2023, **3**, 29.
48 S. S. Karade, S. S. Raut, H. B. Gajare, P. R. Nikam, R. Sharma and B. R. Sankapal, *J. Energy Storage*, 2020, 101622.
49 T. Zahra, M. M. Alanazi, S. A. M. Abdelmohsen, S. D. Alahmari, M. Abdullah, S. Aman, A. Dahshan, A. M. A. Henaish, Z. Ahmad and H. M. Tahir Farid, *Ceram. Int.*, 2024, **50**, 14469–14479.
50 F. H. Albaqal, Z. N. Al Mubarak, F. A. Almomen, J. M. Albarak, N. Y. Aldaleeli, M. Madani, M. S. Attia and M. M. Ghobashy, *ECS J. Solid State Sci. Technol.*, 2025, **14**, 051004.
51 H. Gul, A. U. H. A. Shah, U. Krewer and S. Bilal, *Nanomaterials*, 2020, **10**, 118.
52 P. K. Katkar, S. J. Marje, S. S. Pujari, S. A. Khalate, P. R. Deshmukh and U. M. Patil, *Synth. Met.*, 2020, **267**, 116446.
53 J. Huang, *Electrochim. Acta*, 2018, **281**, 170–188.
54 E. H. Balaguera and A. Allagui, *J. Energy Storage*, 2024, 111801.
55 A. C. Lazanas and M. I. Prodromidis, *ACS Meas. Sci. Au*, 2023, **3**, 162–193.
56 Y. Wang, X. Zhao and Z. H. Liu, *RSC Adv.*, 2020, **10**, 7134–7145.
57 C. Cougnon, *Energies*, 2023, 5687.
58 V. S. Bhat, S. Supriya, T. J. Jayeoye, T. Rujiralai, U. Sirimahachai, K. F. Chong and G. Hegde, *Nano Sel.*, 2020, **1**, 226–243.
59 F. O. Ochai-Ejeh, A. Bello, J. Dangbegnon, A. A. Khaleed, M. J. Madito, F. Bazegar and N. Manyala, *J. Mater. Sci.*, 2017, **52**, 10600–10613.
60 M. Ashraf, S. S. Shah, I. Khan, M. A. Aziz, N. Ullah, M. Khan, S. F. Adil, Z. Liaqat, M. Usman, W. Tremel and M. N. Tahir, *Chem. – Eur. J.*, 2021, **27**, 6973–6984.
61 E. Taer, D. K. H. Tampubolon, Apriwandi, R. Farma, R. N. Setiadi and R. Taslim, *J. Phys.: Conf. Ser.*, 2021, 2462–2475.
62 S. Rajeevan, S. John, D. Ponnamma and S. C. George, *J. Energy Storage*, 2022, 105919.
63 M. Lao, P. Li, Y. Jiang, H. Pan, S. X. Dou and W. Sun, *Nano Energy*, 2022, DOI: 10.1016/j.nanoen.2022.107231.
64 J. B. Jorcin, M. E. Orazem, N. Pébère and B. Tribollet, *Electrochim. Acta*, 2006, **51**, 1473–1479.
65 N. Singh, S. Tanwar, A. L. Sharma and B. C. Yadav, *Int. J. Hydrogen Energy*, 2022, 5–10.
66 V. Sunil, B. Pal, I. Izwan Misnon and R. Jose, *Mater. Today Proc.*, 2020, **46**, 1588–1594.
67 G. Li, Q. Li, J. Ye, G. Fu, J. J. Han and Y. Zhu, *J. Solid State Electrochem.*, 2017, **21**, 3169–3177.
68 X. Li, L. Guo, S. Sun, X. Zhang, G. Liu, H. Yao, M. Shi, J. Li, X. Yu and S. Zhang, *J. Nanosci. Nanotechnol.*, 2017, **17**, 6655–6661.
69 N. A. Khan, Z. Jahan, N. Iqbal, M. B. Niazi and R. Mehek, *Waste Manag.*, 2025, **191**, 274–283.
70 M. O. Bello, N. Abdus-Salam, F. A. Adekola and U. Pal, *Chem. Data Collect.*, 2021, 100607.
71 S. Thior, V. N. Kitenge, K. O. Otun, R. A. M. Adam, N. F. Diop, B. D. Ngom and N. Manyala, *New J. Chem.*, 2024, **49**, 2129–2142.